Energy & Environmental Science

REVIEW

View Article Online
View Journal | View Issue

Cite this: *Energy Environ. Sci.*, 2014, **7**, 2518

Advancements in perovskite solar cells: photophysics behind the photovoltaics

Tze Chien Sum*[a] and Nripan Mathews*[bcd]

Received 27th February 2014
Accepted 1st May 2014

DOI: 10.1039/c4ee00673a

www.rsc.org/ees

Solution-processed organic–inorganic perovskite solar cells are hailed as the recent major breakthrough in low-cost photovoltaics. Power conversion efficiencies approaching those of crystalline Si solar cells (exceeding 15%) have been reported. Remarkably, such phenomenal performances were achieved in a matter of 5 years – up from ~3.8% back in 2009. Since then, the field has expanded exponentially. In this perspective, we review the basic working mechanisms of perovskite solar cells in relation to their intrinsic properties and fundamental photophysics. The current state-of-the-art and the open questions in this maturing field are also highlighted.

Broader context

Organic–inorganic perovskite solar cells have recently emerged as the forerunner in the next generation photovoltaic technology. They have been hailed as one of the major scientific breakthroughs in 2013. Power conversion efficiencies (PCEs) exceeding 15% from these cells have been reported, leapfrogging many other technologies. The wide range of efficient perovskite solar cell device architectures demonstrated points towards a remarkable semiconducting material with excellent electrical and optical properties. As the field matures, a clear understanding of the fundamental photophysical processes and the basic working mechanisms in these perovskite solar cells become increasingly important for further improvements of their PCEs. Towards this direction, the review examines the intrinsic physical and electronic properties of this class of organic–inorganic perovskites as well as its meteoric rise as a photovoltaic material – distilling the findings of recent photophysical studies and highlighting the open questions and future directions of the field in the process.

1. Introduction

Solar power is the world's most abundant energy resource. A year's worth of sunlight contains 1.5×10^{18} kW h of energy. By comparison, the known reserves of oil, coal, and gas are 1.75×10^{15} kW h, 1.4×10^{15} kW h, and 5.5×10^{15} kW h, respectively. Thus, a year's worth of sunlight provides more than a hundred times the energy of the world's entire known fossil fuel reserves. Harnessing solar power would yield a never-ending energy supply.[1] The difficulty has always been converting solar energy in an efficient and cost-effective way. Photovoltaic cells are the most promising avenue for directly converting the photons to electricity. For photovoltaic energy to become competitive with fossil fuels and to capture a significant share of the electricity market, it is necessary to reduce the total cost of solar energy. This can be achieved by either reducing the cost of photovoltaic cells or by increasing their power conversion efficiencies.

The photovoltaic market is currently dominated by crystalline Si solar cells with efficiencies close to 20%. Alternative "third generation" technologies such as organic photovoltaics (OPVs), dye sensitized solar cells (DSCs) and quantum dot solar cells (QDSCs), which are fabricated through solution based processes such as blade coating, screen printing and spraying, promise low cost solar power while allowing the utilization of unconventional substrates. Although the utilization of low temperature processes reduces the energetic costs and the energy payback time, the power conversion efficiencies (PCEs) of these solar cells still lag significantly behind conventional solar cells. The levelized cost of energy (LCOE), which allows for the comparison of various electricity generation sources, depends critically on the efficiency of the solar cells produced.[2] A more efficient module yields more power per unit area. A significant fraction of a solar cell cost scales proportional to the installation area, including the cost of the glass, inverter costs and installation costs, among others. A more efficient solar cell allows for a reduction in all the costs associated with installation, while requiring much lower numbers of solar panels to be installed. Thus the PCE is a primary driver of cost for solar cells.

Organic–inorganic halide perovskite solar cells have been the most significant development in the field of photovoltaics in the present decade and are the best bet at satisfying the

[a]*Division of Physics and Applied Physics, School of Physical and Mathematical Sciences, Nanyang Technological University, 21 Nanyang Link, Singapore 637371. E-mail: Tzechien@ntu.edu.sg*

[b]*School of Materials Science and Engineering, Nanyang Technological University, Nanyang Avenue, Singapore 639798. E-mail: Nripan@ntu.edu.sg*

[c]*Energy Research Institute @NTU (ERI@N), Research Techno Plaza, X-Frontier Block, Level 5, 50 Nanyang Drive, Singapore 637553*

[d]*Singapore-Berkeley Research Initiative for Sustainable Energy, 1 Create Way, Singapore 138602, Singapore*

need for high efficiencies while allowing for low cost solution based manufacturing. Since the first reports of stable solid state solar cells based on the $CH_3NH_3PbI_3$ perovskite in mid-2012, the PCEs of the solar cells have already exceeded 15%, leapfrogging every other solution-processed solar cell technology. The wide range of efficient perovskite solar cell device architectures demonstrated points towards a remarkable semiconducting material with excellent electrical and optical properties. Early pioneering work[3,4] in the area of organic–inorganic halides has clearly shown that this class of materials can behave as low dimensional electronic systems with tunable properties, allowing for the development of newer perovskite solar materials in addition to $CH_3NH_3PbI_3$.

This review focuses on the recent developments (*i.e.*, up to Feb 2014) in perovskite solar cells as well as their photophysical properties and charge dynamics. We first review the intrinsic physical and electronic properties of this class of organic–inorganic perovskites, followed by its progress as a photovoltaic material. The review then examines the recent photophysical studies on unraveling the charge dynamics and transport mechanisms in both perovskite thin films as well as in perovskite solar cells. Due to the rapid pace of research in this area, this review does not aim to be comprehensive but will highlight key studies and findings. Lastly, we conclude the review with the open questions facing these classes of solar cells and future directions of research.

2. Intrinsic properties of organic–inorganic perovskites

(a) Physical structure

Perovskite is the common nomenclature for compounds with the generic chemical formula – AMX_3. In the cubic unit cell, the A-cation resides at the eight corners of the cube, while the M-cation is located at the body center that is surrounded by 6 X-anions (located at the face centers) in an octahedral $[MX_6]^{4-}$ cluster. Typical inorganic perovskites include $CaTiO_3$ and $SrTiO_3$. Due to the interplay of the charge, spin and structural properties, this family of materials is known to exhibit a plethora of novel and exciting phenomena such as superconductivity, magnetoresistance, ferroelectricity, magnetoelectricity, anti-ferromagnetism, anti-ferroelectricity, *etc.*[5] In the classes of compounds being discussed here, the A cations are organic (typically $CH_3NH_3^+$, $C_2H_5NH_3^+$, $HC(NH_2)_2^+$), the metal cations (M) are typically divalent metal ions such as Pb^{2+}, Sn^{2+}, Eu^{2+}, Cu^{2+} *etc.*, while the X anions are halides (Cl^-, Br^-, I^-). $CH_3NH_3PbI_3$ belongs to a large family of organic–inorganic perovskites where the $[PbI_6]^{4-}$ octahedral can form three-dimensional (3-D), two-dimensional (2-D), one-dimensional (1-D) or zero-dimensional (0-D) networks, possessing the same unit structure – Fig. 1. The absence of any inhomogeneous broadening (arising from the size distribution of the samples) in these 3-D and their low-dimensional counterparts makes these compounds ideal for investigating quantum confinement effects on semiconductor mesoscopic structures. Pioneering work in this class of compounds began as early as 1989 where

Dr Tze-Chien Sum is an Assistant Professor at the Division of Physics and Applied Physics, School of Physical and Mathematical Sciences, Nanyang Technological University (NTU) where he leads the Femtosecond Dynamics Laboratory. He received his PhD in 2005 from the National University of Singapore, where he worked on the development of a new direct-write lithographic technique (proton beam writing) for photonic applications. Upon joining NTU in 2005 as a lecturer, he switched to the exciting field of ultrafast optical spectroscopy or femtosecond time-resolved spectroscopy and established the xC-Lab research group – a lab for investigation of exCited-state phenomena. His research focuses on investigating light–matter interactions; energy and charge transfer mechanisms; and probing carrier and quasi-particle dynamics in a broad range of emergent nanoscale and light harvesting systems using femtosecond time-resolved spectroscopy.

Dr Nripan Mathews is an assistant professor at the School of Materials Engineering in Nanyang Technological University. He pursued his PhD at a joint Commissariat à l'énergie atomique (CEA) – Centre national de la recherche scientifique (CNRS) – Universite de Pierre et Marie Curie (Paris VI University) laboratory in the area of molecular crystals, studying the signatures of optical excitations within them (2008). He was also a visiting scientist at Prof. Michael Grätzel's laboratory at École Polytechnique Fédérale de Lausanne (EPFL), working on a pan-european project on photoelectrochemical hydrogen production. His research focuses on a wide variety of novel materials (metal oxides, organic semiconductors, graphene, carbon nanotubes, sulfides, and selenides) and novel morphologies (one dimensional structures such as nanowires and nanotubes, thin films as well as two dimensional nanosheets) produced through a range of fabrication procedures. He has focussed primarily on the electronic and optical properties of these materials and how they can be adapted for practical applications.

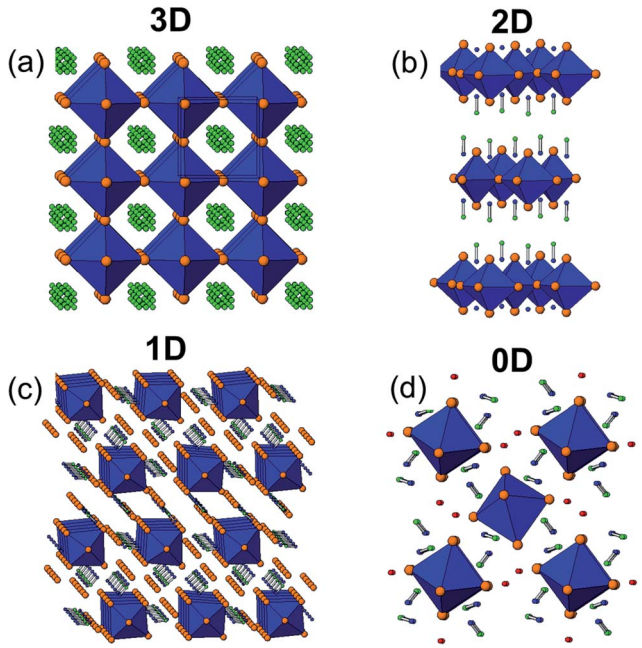

Fig. 1 Crystal structures of (a) $CH_3NH_3PbI_3$,[21] (b) $(CH_3NH_3)_2PbI_4$,[19] (c) $(C_{10}H_{21}NH_3)_2PbI_4$,[20] and (d) $(CH_3NH_3)_4PbI_6\cdot 2H_2O$,[22] corresponding to 3D, 2D, 1D and 0D networks. The blue polyhedra represent the MX_6 (M = Pb, Sn and Cu; X = I and Br) octahedra with the halogens represented by orange spheres – the building blocks of these compounds. The blue, green and red spheres are the N, C and O, respectively (H atoms were removed for clarity). The ID network extends into the plane of the document.

the focus was on the effects of dimensionality on the excitonic, optical and electronic properties.[4,6,7] The optoelectronic properties of layered organic–inorganic perovskites were also extensively studied because of the novel properties exhibited by these crystals which include: high mobilities for thin-film transistors;[8,9] strong excitonic properties for light emitting diodes;[10,11] large nonlinearities with ultrafast responses;[12,13] and even polariton emission in 2D perovskite-based microcavities.[14–18]

In $CH_3NH_3PbI_3$, each $[PbI_6]^{4-}$ octahedron is connected with six neighbours at the iodide – forming a 3-D network (Fig. 1(a)). The countercation ($CH_3NH_3^+$) is located at the void of the network. For the 2-D case[19] *e.g.*, $(CH_3NH_3)_2PbI_4$, each $[PbI_6]^{4-}$ octahedron is connected with four neighbours at the halide – forming a 2-D network layer that is sandwiched between two $CH_3NH_3^+$ layers (also not shown in Fig. 1(b)). A multiple quantum well structure results from the stacking of these sandwiched layers *via* van der Waals interaction – with the 2-D $[PbI_6]^{4-}$ functioning as the quantum well and the $CH_3NH_3^+$ layer as the barrier. For the 1-D case[20] (*e.g.*, $(C_{10}H_{21}NH_3)_2PbI_4$), each octahedron is connected at two opposite corners with its neighbour – forming separate infinite chains – Fig. 1(c). Lastly, the quantum dot (0-D) analogue manifests as $(CH_3NH_3)_4PbI_6\cdot 2H_2O$, where each $[PbI_6]^{4-}$ complex is neutralized by four $CH_3NH_3^+$ ions to form a molecule – Fig. 1(d). A quantum dot array results when these molecules are isolated by H_2O molecules to form a molecular crystal.

(b) Electronic structure

Early studies on the electronic band structures of organic–inorganic (3-D and low-dimensional) perovskites can be traced to the studies of: Koutselas *et al.*[7] using band structure calculations by a semi-empirical method based on the extended Hückel theory and an *ab initio* approach based on the Hartree–Fock theory; T. Umebayashi *et al.*[23] using ultraviolet photoelectron spectroscopy and first principles density functional theory (DFT) band calculations for the room temperature cubic phase; and Chang *et al.*[24] using first principles pseudopotential calculations. DFT calculations for the 3-D $CH_3NH_3PbI_3$ crystal revealed that the valence band maxima comprises the Pb 6p–I 5p σ-antibonding orbital, while the conduction band minima consists of Pb 6p–I 5s σ anti-bonding and Pb 6p–I 5p π anti-bonding orbitals (see Fig. 2 below).[23]

Following the attention garnered by perovskite solar cells, renewed interest in the DFT studies of 3-D perovskites began in earnest. In the work of E. Mosconi together with F. De Angelis and their collaborators,[25] they calculated the band structure for $CH_3NH_3PbX_3$ (cubic phase) and the mixed halide $CH_3NH_3PbI_2X$ (tetragonal phase) (X = Cl, Br and I) with the surrounding $CH_3NH_3^+$ counterions, which were ignored in the earlier studies. Nevertheless, the organic component had little influence on the bandgap energy, of which is mainly determined by the $[PbI_4]^{6-}$ network. In addition, the authors highlight that the

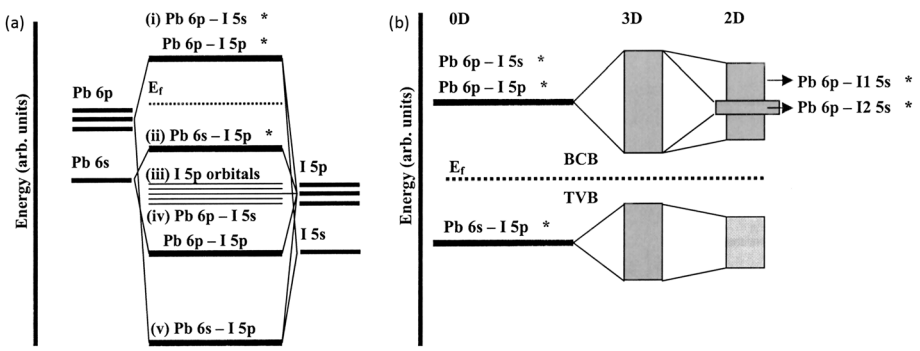

Fig. 2 Bonding diagram of (a) $[PbI_6]^{4-}$ cluster (0-D), (b) $CH_3NH_3PbI_3$ (3-D) and (b) $(C_4H_9NH_3)_2PbI_4$ (2-D) at the top of the valence band and at the bottom of the conduction band. Reproduced with permission from ref. 23 copyright 2003, American Physical Society (APS).

close matching of their calculated bandgaps (where spin-orbit coupling (SOC) effect were not considered) with the experimental data is likely to be fortuitous. These findings are consistent with the studies by T. Baikie *et al.*[26] and Y. Wang *et al.* (low-temperature orthorhombic phase).[27] Investigation on the SOC effect on the electronic band structure in 3-D perovskites (low-temperature orthorhombic phase) was reported by J. Even *et al.*,[28] where they found that the SOC dramatically reduces the energy gap affecting mainly the conduction band.

Having covered the fundamental properties of the large family of organic–inorganic perovskites, we next focus our attention on $CH_3NH_3PbI_3$ and their photovoltaic applications.

3. Progress in perovskite photovoltaics

Initial studies in the area of perovskite solar cells arose as an evolution of the dye sensitized solar cell[29] architecture. DSCs typically consist of a mesoporous n-type TiO_2 electrode which has been sensitized by a dye and placed in a liquid electrolyte (typically the I^-/I_3^- redox couple). Since the grafted dyes only form a monolayer, the mesoporous electrode must be 10–15 μm thick to enable complete light absorption. The development of alternative semiconducting sensitizers (either in a thin film or QD form) allows for a reduction in the mesoporous TiO_2 layer thickness. Miyasaka and coworkers[30] in 2009 demonstrated the first perovskite sensitized solar cells utilizing $CH_3NH_3PbI_3$ and $CH_3NH_3PbBr_3$ as light absorbers on TiO_2 mesoporous layers with halide electrolytes. A significant efficiency of 3.81% was obtained from $CH_3NH_3PbI_3$ with photocurrent onset observed from ~800 nm. An impressive photovoltage of 0.96 V was obtained from $CH_3NH_3PbBr_3$, attributed to the deeper bromide redox couple used in such solar cells. Further improvements[31] in such liquid electrolyte solar cells were made by N. G. Park and coworkers in 2011 through a careful optimization of the mesoporous layer thickness, perovskite concentration and surface treatment. Surface modification of TiO_2 with $Pb(NO_3)_2$ prior to deposition of perovskites resulted in an efficiency of 6.54% (J_{SC} = 15.82 mA cm^{-2}, V_{OC} = 0.706 V and FF = 0.586). Despite the efficiencies achieved in such configurations, the overall instability of the solar cells due to the dissolution of the perovskite in the liquid electrolyte appeared to be a challenge.

A breakthrough in both efficiency and stability was achieved in 2012 through utilization of a solid-state hole transporter 2,2′,7,7′-tetrakis(*N*,*N*-*p*-dimethoxy-phenylamino)-9,9′-spirobifluorene (spiro-OMeTAD) with $CH_3NH_3PbI_3$ and $CH_3NH_3PbI_{3-x}Cl_x$ as light absorbers (Fig. 3).[32,33] N. G. Park, M. Grätzel and coworkers reported a PCE of 9.7% (J_{SC} = 17.6 mA cm^{-2}, V_{OC} = 0.888 V and FF = 0.62) for $CH_3NH_3PbI_3$ on 0.6 μm TiO_2 layers. The use of spiro-OMeTAD dramatically improved the device stability compared to liquid junction cells with *ex situ* long-term stability tests conducted for over 500 h, where the devices are stored in air at room temperature without encapsulation.[32] H. Snaith and coworkers on the other hand utilized a mixed halide system – $CH_3NH_3PbI_{3-x}Cl_x$ on both TiO_2 and Al_2O_3 mesoporous layers. Incredibly, the highest efficiencies (PCE = 10.9%, J_{SC} = 17.8 mA cm^{-2}, V_{OC} = 0.98 V and FF = 0.63) were obtained for the mesoporous Al_2O_3 devices where they act purely as scaffolds and do not take part in the electrical processes.[33] These concurrent reports sparked an explosion of research activities where a variety of device configurations, deposition protocols and material sets have been employed.

(a) Device architectures

A common device configuration for $CH_3NH_3PbI_3$ based solar cells consists of infiltrating the perovskite within an n-type

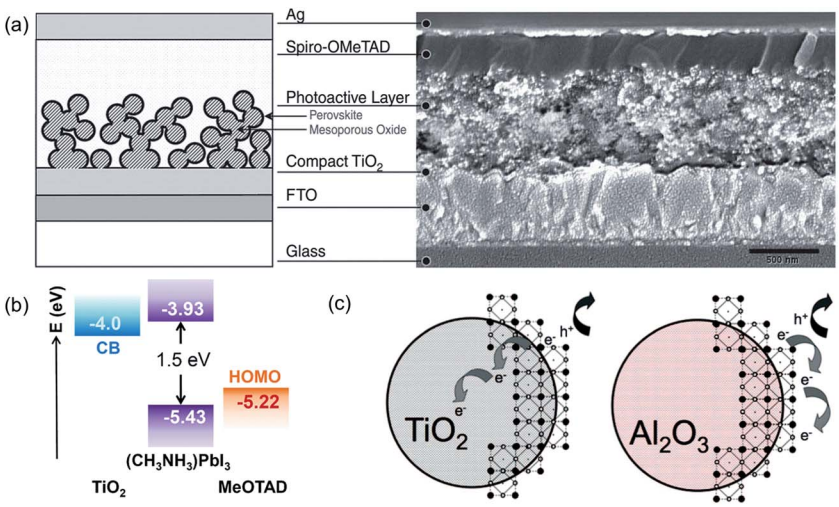

Fig. 3 (a) Schematic illustrating mesoporous perovskite solar cells. The mesoporous oxide can be an electron transporting semiconductor such as TiO_2, ZnO or an insulating layer such as Al_2O_3 or ZrO_2 (meso-superstructured solar cell – MSSC); (b) relevant energy levels in the mesoporous TiO_2 perovskite solar cells; (c) schematic illustrating the charge transfer and charge transport in a perovskite TiO_2 solar cell and a non-injecting Al_2O_3 based solar cell; (a) and (c) are reproduced from ref. 33 copyright 2012, Science (AAAS) and (b) is reproduced from ref. 32 copyright 2012, Nature Publishing Group.

mesoporous layer (Fig. 3(a)). The solar cell fabrication process commences with the deposition of a compact TiO_2 hole-blocking layer on top of the fluorine doped tin oxide (FTO) substrate. This is typically done through the spray pyrolysis of precursors such as titanium diisopropoxide bis(acetylacetonate) at ~450 °C. It is important to ensure that the compact layer is pinhole-free and uniform to prevent the recombination between carriers from the perovskite layers and FTO. On top of the compact layer, a mesoporous layer of n-type TiO_2 is formed either by screen printing or spincoating a nanoparticle TiO_2 paste followed by annealing to remove the polymeric binders. The thickness and porosity of these layers can be modulated by changing the filler and solvent concentrations in the TiO_2 paste. The perovskite films are then deposited on top of the n-type mesoporous layer by spincoating it from a solvent such as γ-butyrolactone (GBL) or *N*,*N*-dimethylformamide (DMF). This is followed by the deposition of a hole transporting material (HTM) such as spiro-OMeTAD with appropriate dopants to improve conductivity. Finally, a metal electrode is deposited on top of the HTM to complete the solar cell.

Although TiO_2 nanoparticles are most commonly used,[32,34–37] there have also been reports of solar cells employing TiO_2 nanosheets,[38] nanorods,[39] nanofibers[40] as well as other n-type materials such as ZnO.[41,42] Despite the wide variety of mesoporous architectures being employed, there has been no clear evidence that the efficiencies of the perovskite solar cells can be effectively increased by mesoporous layer modification. The most significant effect of the mesoporous layer that has been noted is how their thicknesses can affect the power conversion efficiencies. Both in the liquid junction configuration, as well as in its solid state equivalent, it has been demonstrated that lower mesoporous layer thicknesses perform better.[31,32,39] The highest efficiencies in these kinds of configurations have been obtained with a 350 nm thick mesoporous TiO_2 layer infiltrated with $CH_3NH_3PbI_3$.[35] The high efficiencies of these solar cells at relatively low TiO_2 thicknesses (in contrast to ~3 μm thickness for solid state DSCs[43] and 10–15 μm thickness for DSCs[44]) can be traced to the high optical absorption coefficient (~10^5 cm^{-1}) of $CH_3NH_3PbI_3$.[31,45,46] The exact dependence of the mesoporous layer thickness on the PCE is determined by the nature of the perovskite distribution within the TiO_2 layers[47] as well as the perovskite overlayer thickness[34] (which is in turn dependent on the perovskite solution concentration). The demonstration of good efficiencies[39] in rutile TiO_2 nanowires, which have been shown to perform poorly in DSCs (due to poor electron transport),[48] again indicates that the thickness of the mesoporous layer is a more critical factor. An interesting change in this device configuration stems from the work of Etgar and coworkers who have demonstrated that such mesoporous TiO_2 based solar cells do not require a HTM to function.[38,49] The initial study employed anatase TiO_2 nanosheets as the mesoporous layer,[38] onto which the perovskite layers were spuncoated and followed by the evaporation of a gold electrode. The solar cells so fabricated displayed an efficiency of 5.5% (J_{SC} = 16.1 mA cm^{-2}, V_{OC} = 0.63 V and FF = 0.57). Further optimization of the perovskite layer thickness through consecutive spincoating resulted in an efficiency of 8%.[49] The successful functioning of such devices indicate that $CH_3NH_3PbI_3$ can act as an effective hole transporter. However, the V_{OC}s of such devices are lower than that produced with spiro-OMeTAD indicating that the lack of the electron selection layer results in increased recombination.

Another efficient solar cell configuration that has been chiefly employed by Snaith and coworkers is the meso-superstructured solar cell (MSSC). This device configuration employs an insulating mesoporous layer on top of the compact TiO_2 layer as a scaffold to load the perovskite within them. Much of the reports employing this configuration utilize Al_2O_3 as the mesoporous layer and the mixed perovskite $CH_3NH_3PbI_{3-x}Cl_x$ as the absorber.[33,50–52]

However, the high efficiencies observed in this device configuration are not specific to this material combination. Hagfeldt and coworkers have also demonstrated efficient solar cells (PCE = 10.8%, J_{SC} = 17.3 mA cm^{-2}, V_{OC} = 1.07 V and FF = 0.59) by employing $CH_3NH_3PbI_3$ deposited on an insulating ZrO_2 mesoporous layer.[36] The lack of an n-type mesoporous layer in this device configuration clearly indicates that efficient electron transport occurs within the perovskite itself (Fig. 3 (c)). This also indicates that the perovskite within the mesoporous layer is continuous, in contrast to previous studies which had considered them as isolated quantum dots.[30,31] The contrast between both the views could be explained by recent work,[47] which indicated that $CH_3NH_3PbI_3$ exists as two components within the mesoporous TiO_2, one component with medium range crystalline order (30 atom%) and another with only local structural coherence (70 atom%). The electron transporting nature of the perovskite is further highlighted in the work of Ball *et al.*[50] By thinning down the Al_2O_3 scaffold thickness (Fig. 4(a)), the authors were able to form solar cells which appeared more as thin film solar cells. The J_{SC} for such solar cells were 16.9 ± 1.9 mA cm^{-2} for thin alumina scaffold layers (80 nm) indicating that thick perovskite films could generate sufficient photocurrent. The ability of the perovskites to be employed in such electron transporter-free configuration, as well as to perform efficiently in an HTM-free configuration,[38,49] points towards the ambipolar nature of transport in them. However, it is important to note that the MSSCs do not have the reduced V_{OC}s associated with the HTM-free solar cells primarily

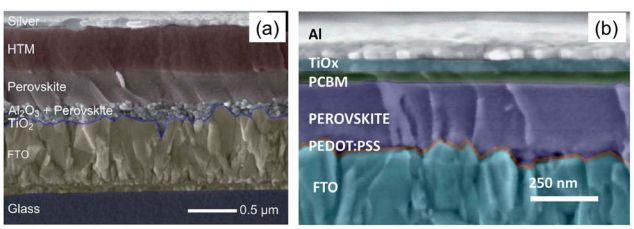

Fig. 4 (a) Cross-sectional SEM view of a "pseudo-thin film" architecture employing a thin Al_2O_3 mesoporous layer with a significantly thick perovskite film over it; (b) cross-sectional view of a planar perovskite solar cell illustrating the typical organic charge transport layers employed. (a) is reproduced from ref. 50 copyright 2013, Royal Society of Chemistry. (b) is reproduced from ref. 53 copyright 2013, Nature Publishing Group.

due to the presence of the hole selective contacts. The effects of carrier accumulation within the perovskite could also be a possible reason for the enhanced V_{OC}s.

The success of the "pseudo-thin film" MSSC solar cells has driven explorations into planar thin film configurations of the perovskite solar cells. Thin film solar cells allow for a simpler processing route. One approach to realize such thin film solar cells is to avoid the use of any mesoporous layer and deposit the films directly on the TiO_2 compact layer. The initial report on MSSCs had included results from a planar configuration (FTO/compact TiO_2/$CH_3NH_3PbI_{3-x}Cl_x$/spiro-OMeTAD/Ag), but with a relatively low efficiency of 1.8%.[33] The difficulties associated with the fabrication of a thin film solar cell stem from the challenges of depositing a homogeneous pin-hole free perovskite layer through solution based processes. Poor coverage results in poor light absorption as well as shunting paths through the light absorber layer which reduces efficiency. Unlike polymeric films which are mostly amorphous when deposited by spincoating, perovskites are crystalline. Even mild heating to remove solvent residues can result in dewetting and roughening of the as deposited perovskite film. Eperon *et al.* have carefully studied the morphological effects of the underlying substrate, annealing time, temperature and initial perovskite($CH_3NH_3PbI_{3-x}Cl_x$) film thickness. Through control of the various factors involved, the authors achieved an efficiency of 11.4% ($J_{SC} = 20.3$ mA cm^{-2}, $V_{OC} = 0.89$ V and FF = 0.64).[54] A much simpler approach[55] involved the vapour deposition of the perovskite films onto the TiO_2 films which yielded a short-circuit photocurrent of 21.5 mA cm^{-2}, an open-circuit voltage of 1.07 V and a fill factor of 0.68, and an efficiency of 15.4%. An interesting vapour-assisted approach to form efficient planar solar cells has also been demonstrated by Yang and coworkers.[56] A 350 nm thick $CH_3NH_3PbI_3$ film formed on the compact TiO_2 layer yielded an efficiency of 12.1%, despite the relatively thick HTM layer employed in the devices. A similar planar solar cell approach, which allows for low temperature processing, involves the utilization of ZnO as the blocking layer. The first approach by Kumar *et al.* employed electrodeposited ZnO on both rigid FTO and flexible ITO on top of which $CH_3NH_3PbI_3$ was spuncoated.[41] The second approach utilized spuncoated films from a solution of 5 nm ZnO nanoparticles suspended in a butanol–chloroform mixture requiring no calcination or sintering. The authors argue that the lack of a constricting mesoporous layer allows for unconstrained $CH_3NH_3PbI_3$ perovskite crystal growth yielding an impressive efficiency of 15.7% on FTO and 10.2% on flexible ITO substrates.[57]

Another growing area of research involves the use of electron and hole transport layers commonly utilized by the organic photovoltaic community for the implementation of the planar solar cell configuration. The first work in this direction was performed by Chen and coworkers who employed a device architecture consisting of poly(3,4-ethylenedioxythiophene):poly(styrenesulfonic acid) (PEDOT:PSS) as the hole transport layer and C_{60} derivatives including (6,6)-phenyl C61-butyric acid methyl ester (PCBM) and indene-C_{60} bisadduct (ICBA) as the electron transporters in a planar configuration.[58] As with forming perovskites on top of TiO_2 thin films, the authors faced challenges in forming a uniform $CH_3NH_3PbI_3$ coating on top of the PEDOT:PSS layer. This restricted the total thickness of the $CH_3NH_3PbI_3$ utilized, hence limiting the efficiencies to 3.9%. Sun *et al.* employed a similar device configuration but succeeded in making a thicker $CH_3NH_3PbI_3$ (110 ± 5 nm) film through the utilization of a two-step conversion approach. The highest efficiency reported in such a device was 7.41%.[45] Snaith and coworkers[53] screened a wider material set employed in OPVs, including NiO and V_2O_5 hole transport layers and poly[(9,9-bis(30-(*N*,*N*-dimethylamino)propyl)-2,7-fluorene)-*alt*-2,7-(9,9-dioctylfluorene)] (PFN) as an electron selective contact with $CH_3NH_3PbI_{3-x}Cl_x$. However, the most efficient device configuration still employed $PC_{61}BM$ and PEDOT:PSS as the two previous reports covered above. A ~300 nm thick $CH_3NH_3PbI_{3-x}Cl_x$ layer (Fig. 4(b)) yielded an efficiency of 9.8% while flexible solar cells were also fabricated on ITO coated glass yielding 6.3%. Crucially, the lower efficiencies on the flexible devices were attributed to the smoother surface of the ITO layer which affects the uniformity of the perovskite coating. However, even higher efficiencies have been demonstrated for flexible $CH_3NH_3PbI_{3-x}Cl_x$ solar cells on ITO by Yang and coworkers (9.2%).[59]

(b) Deposition processes

Much of the initial work on $CH_3NH_3PbI_3$ and $CH_3NH_3PbI_{3-x}Cl_x$ solar cells utilized spincoating to deposit the light absorbers from a single precursor solution. $CH_3NH_3PbI_3$ films were formed by dissolving stoichiometric quantities of CH_3NH_3I and PbI_2 in polar solvents such as GBL or DMF.[32,34] $CH_3NH_3PbI_{3-x}Cl_x$ is typically formed from a solution in DMF where the $PbCl_2$ and CH_3NH_3I are in a molar ratio of 1 : 3.[33,50] With appropriate optimization of the precursor concentration and spincoating conditions, the perovskite can be deposited within the pores of the mesoporous layers or be used to form compact layers for planar solar cells. As described previously, the formation of a uniform perovskite layer for planar devices through spincoating requires the optimization of multiple parameters including post-deposition processes.[45,54,58] Due to wettability differences, the perovskite would need to be separately optimized for each underlying layer. When spincoating on mesoporous layers, conditions similar to the deposition of HTMs within the mesoporous TiO_2 layers of a solid state DSC could be expected to occur.[60] In such a case, the excess solution on top of the film can act as a reservoir during the spincoating process. The amount of infiltration within the mesoporous layer would depend critically on the solution concentration, spincoating speed and the solvent utilized. The tendency of the perovskite films to crystallise, could lead to rough surface morphologies[34] which could introduce shunts into the solar cells.

A significant development for solution based deposition has been the application of the sequential deposition process (originally developed by Mitzi and coworkers[61]) for the fabrication of perovskite solar cells by Grätzel and coworkers.[35] The process consists of first spincoating PbI_2 on the TiO_2 layer from a solution under appropriate conditions (solution concentration, spincoating speed) to enable infiltration within the mesoporous layer (Fig. 5(a)). Subsequently, the yellow coloured

substrates are dipped in a CH_3NH_3I solution in 2-propanol solvent. During the dipping, the yellow PbI_2 converts to form the dark brown $CH_3NH_3PbI_3$ in a few seconds (Fig. 5(b)). It is important to note that the conversion time can vary between the different PbI_2 deposition conditions. A 20 minute conversion time has been reported for perovskite solar cells,[40] while the initial work by Mitzi and coworkers indicated that the conversion required 1–3 h.[61] It is likely that the PbI_2 layer deposited on top of mesoporous substrates has increased roughness that allows the conversion reaction to proceed faster.[35] Due to the volume expansion[56] (~75%) occurring due to the conversion of PbI_2 into $CH_3NH_3PbI_3$, it can be expected that the mesoporous layer would be better infiltrated through the sequential deposition process. The top view of the sequentially deposited samples reveals a highly crystalline film with complete coverage (Fig. 5(c)).

Apart from the widely utilised solution based deposition processes, vapour deposition has also been employed to form perovskite solar cells. Snaith and coworkers[55] demonstrated efficient planar solar cells (15.4%) of $CH_3NH_3PbI_{3-x}Cl_x$ formed by dual source evaporation of $PbCl_2$ and CH_3NH_3I (Fig. 5(e)). The evaporated film was sandwiched between a compact TiO_2 layer and a spuncoated spiro-OMeTAD layer acting as electron and hole transporters, respectively. The vapour-deposited films are extremely uniform, with crystalline features on the length scale of hundreds of nanometres. Another example of vapour deposition was demonstrated by Bolink and coworkers[62] who deposited thin films of $CH_3NH_3PbI_3$ from the dual source evaporation of PbI_2 and CH_3NH_3I. The authors employed organic electron and hole transport layers such as PCBM and PEDOT:PSS to form solar cells with 12.04% efficiency. Both the dual source evaporation examples described above required careful optimization to yield the desired perovskite layers and efficient solar cells. An interesting approach which employs both solution based deposition and vapour phase transformation has been reported by Chen *et al.*[56] In the vapour-assisted solution process (VASP), PbI_2 was first deposited from solution onto a compact TiO_2 substrate. Subsequently, the films were exposed to a vapour of CH_3NH_3I at 150 °C in N_2 for 2 h (Fig. 5(d)). The slow rate of conversion resulted in $CH_3NH_3PbI_3$ films which exhibited micron sized grains with very low surface roughness of ~20 nm. Solar cells made from such films exhibited an efficiency of 12.1%.

In conjunction with these exciting device-centric advancements, fundamental studies into the photoexcited species and their photogeneration and recombination dynamics in perovskites also began in earnest. The next section traces these early studies to the latest findings of the fundamental photophysical mechanisms in this system.

4. Photophysical mechanisms in $CH_3NH_3PbI_3$ thin films

The early photophysical studies in this class of organic–inorganic perovskites are mainly centered on the excitonic properties of layered perovskites such as the optical non-linearity around the excitonic resonances[63] and the exciton–exciton interactions.[64] Coherent transient spectroscopy such as four wave mixing has been used to investigate the exciton and bi-exciton dynamics[65] and temperature dependent TRPL spectroscopy for the exciton recombination dynamics[66] in these 2D perovskites. Depending on the exciton binding energy E_b, the fundamental excited species following photoexcitation could exist as bound electron–hole pairs or as free carriers. Hence, E_b have also been extensively investigated for $CH_3NH_3PbI_3$, the photovoltaic material of choice. Table 1 shows the E_b of selected

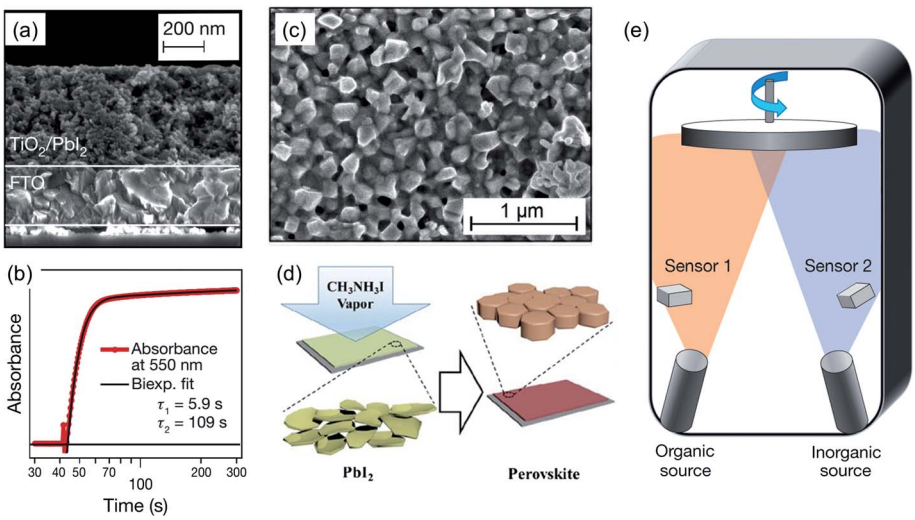

Fig. 5 (a) Cross-sectional SEM of a mesoporous TiO_2 film infiltrated with PbI_2. (b) Change in absorbance at 550 nm of such a film monitored during the transformation from PbI_2 to $CH_3NH_3PbI_3$. (c) Top view of the $CH_3NH_3PbI_3$ film obtained using the sequential deposition method. (d) An illustration of the vapour assisted transformation of PbI_2 to $CH_3NH_3PbI_3$ by exposure to CH_3NH_3I vapour. (e) Dual-source thermal evaporation system for depositing the perovskite absorbers; the organic source was methylammonium iodide and the inorganic source $PbCl_2$. (a–c) are reproduced from ref. 35 copyright 2013, Nature Publishing Group; (d) is reproduced from ref. 56 copyright 2013, American Chemical Society and (e) is reproduced from ref. 55 copyright 2013, Nature Publishing Group.

3-D perovskites with low-dimension perovskites included for comparison. These E_b are estimated using optical absorption[7] and magneto-absorption spectra[67,68] as well as from temperature-dependent photoluminescence (PL) intensities.[45,69] The excitons in $CH_3NH_3PbI_3$ are expected to be of the more delocalized Wannier-type with exciton Bohr radius, $r_B \sim 30$ Å.[7,70] Larger binding energies for $CH_3NH_3PbBr_3$ and the mixed halide $CH_3NH_3PbI_{3-x}Cl_x$ system indicate a more tightly bound nature of the excitons resulting from the halogen substitution. In contrast, for 2-D layered perovskites, the excitons are the Frenkel type and their large binding energies are ascribed to dielectric modulation between the organic and inorganic layers and the two dimensionality of the inorganic structure.[71] With decreasing dimensionality to 1-D and 0-D, the exciton binding energies increase in accordance with the quantum confinement effects.[70]

Absorption of photons creates electron–hole pairs in perovskite. Following carrier thermalization, these carriers could either continue to exist as free carriers or form excitons depending on the exciton binding energy. Presently, it is still unclear whether these species at room temperature exist as excitons or free charges – which gave rise to the 3-D perovskite's exceptional properties of long diffusion lengths. This uncertainty stems from the low exciton binding energies E_b ranging from 19 meV to 50 meV, which are comparable to the room temperature thermal energies of $k_BT \sim 25$ meV. Given the uncertainties and the assumptions involved with the estimation/extraction of the values for E_b based on the various methods employed (optical absorption,[73,74] magneto-absorption[68] and temperature dependent PL[75]), it is reasonable from Table 1 that the E_b for $CH_3NH_3PbI_3$ is comparable to the thermal energies of $k_BT \sim 25$ meV at room temperature. As an illustration, even for an $E_b \sim 19$ meV, the faction of the excitons with an energy greater than E_b at ~300 K can be calculated from statistical physics to yield: ~57% of the photo-generated excitons dissociating spontaneously and ~43% remaining as excitons. It is an open question on how the co-existence of free carriers and excitons, whose dynamic populations could vary over their lifetimes, will affect the carrier dynamics in perovskite solar cells.

Table 1 Exciton binding energies E_b of the 3-D $CH_3NH_3PbI_3$ and $CH_3NH_3PbI_{3-x}Cl_x$ perovskites and selected low-dimension perovskites

Compound	Dimensionality	E_b (meV)	Method
$CH_3NH_3PbI_3$	3D	30	Optical absorption[7]
		37	Magneto-absorption[67]
		45	Temperature dependent PL[69]
		50	Magneto-absorption[68]
		19 ± 3	Temperature dependent PL[45]
$CH_3NH_3PbBr_3$	3D	76	Magneto-absorption[68]
		150	Optical absorption[7]
$CH_3NH_3PbI_{3-x}Cl_x$	3D	98	Temperature dependent PL[72]
$(C_9H_{19}NH_3)_2PbI_4$	2D	≥330	Temperature dependent PL[69]
$(NH_2C(I)=NH_2)_3PbI_5$	1D	≥410	Optical absorption[7]
$(CH_3NH_3)_4PbI_6\cdot 2H_2O$	0D	545	Optical absorption[7]

To the best of our knowledge, there have been no reported studies on the charge dynamics in 3D perovskites until the advent of the 9.7% perovskite solar cells in 2012.[32] Despite the rapid progress in organic–inorganic perovskite solar cells, the fundamental photophysical processes driving the high performance of these devices is still severely lacking. The bulk of the research efforts to date are predominantly focused on device development, with limited studies on charge carrier dynamics in the $CH_3NH_3PbI_3$ perovskite materials.[32,33,46,76–78] Nevertheless, efforts into applying ultrafast optical spectroscopy (UOS) techniques to investigate the structure–function relationships in perovskite solar cells are on the rise. UOS techniques are powerful probes of carrier dynamics and charge transfer mechanisms in materials. A clear understanding of the charge generation and transport mechanisms in perovskite solar cells will provide valuable feedback to guide the materials design and device engineering. Here, we first examine the intrinsic charge dynamics in the bare perovskite thin films. The charge transfer processes in a typical perovskite solar cell will be examined in the next section.

(a) Long electron–hole diffusion lengths and hot hole cooling dynamics

In tandem with the developments of increasing perovskite solar cell efficiencies, indications of ambipolar charge transport in perovskites became apparent when efficient perovskite-based devices in a broad range of device architectures are reported. The perovskite material functions well as an absorber in a configuration used by Kim *et al.*[32] and Heo *et al.*[34] that sandwiches the thin perovskite layer between a mesoporous TiO_2 photoanode and a HTM layer (spiro-OMeTAD). Lee *et al.*[33] demonstrated that the perovskite material can also work effectively as both an absorber and an electron transporter by fabricating solar cells with an insulating Al_2O_3 scaffold instead of the TiO_2 photoanode. Surprisingly, Etgar *et al.*[38] fabricated devices with appreciable performance in a configuration without the HTM layer – indicating that the perovskite material can also work as an absorber and a hole transporter.

These reports provide us with a compelling case to devise quenching experiments utilizing femtosecond transient optical spectroscopy (*i.e.*, TAS and time-resolved PL (TRPL) spectroscopy) of $CH_3NH_3PbI_3$ heterojunctions with selective electron or hole extraction to decouple the electron and hole dynamics in this material.[46] Our findings revealed clear evidence of balanced and long-range electron–hole diffusion lengths of *at least* 100 nm in solution processed $CH_3NH_3PbI_3$ (Fig. 6). Concurrently, using the same PL quenching approach, H. J. Snaith and coworkers[77] also performed diffusion length measurements on $CH_3NH_3PbI_3$ and the mixed halide $CH_3NH_3PbI_{3-x}Cl_x$. Their findings of the electron–hole diffusion lengths in $CH_3NH_3PbI_3$ concur with ours. Amazingly, the mixed halide $CH_3NH_3PbI_{3-x}Cl_x$ possesses diffusion lengths one order longer (*i.e.*, >1 μm) than

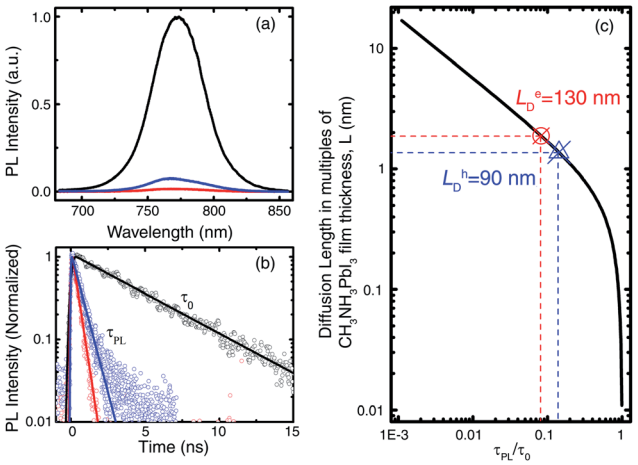

Fig. 6 (A) Time-integrated PL spectra and (B) time-resolved PL decay transients measured at 760 ± 10 nm for quartz/$CH_3NH_3PbI_3$(65 nm) (black), quartz/$CH_3NH_3PbI_3$ (65 nm)/PCBM (red), quartz/$CH_3NH_3PbI_3$(65 nm)/spiro-OMeTAD (blue) films under vacuum after excitation at 600 nm (1 KHz, 150 fs, 1.3 μJ cm^{-2}). The solid lines in (B) are the single-exponential fits of the PL decay transients. a.u.: arbitrary units. (C) A plot of exciton diffusion length *versus* PL lifetime quenching ratios. The diffusion length is scaled in multiples of $CH_3NH_3PbI_3$ layer thickness (L = 65 nm). Reproduced with permission from ref. 46, copyright 2013, Science (AAAS).

$CH_3NH_3PbI_3$, although no clear reason was identified for this difference. Nevertheless, these two studies clearly show that the electron–hole diffusion lengths in perovskites are much longer than those for most solution processed materials (typically ~10 nm). Most recently, G. Giorgi *et al.*'s spin-polarized DFT calculations[79] determined the effective masses of both the electron and hole in $CH_3NH_3PbI_3$ to be small, (*i.e.*, $m_e^* = 0.23m_0$ and $m_h^* = 0.29$), thus providing further validation of their long-range ambipolar charge transport property.[46,77]

In this same work, we also examined the early time relaxation dynamics in the $CH_3NH_3PbI_3$ system. It is important to note that the carrier dynamics in the perovskite system are strongly pump fluence dependent due to their large optical absorption coefficients and long charge diffusion lengths. Multi-particle Auger (third order) recombination processes becomes dominant for pump fluence >2.6 μJ cm^{-2}. In fact, we recently discovered that at a pump fluence >12 μJ cm^{-2}, amplified spontaneous emission (ASE) prevails and even outcompetes the Auger processes.[80] Therefore, careful control of the pump fluence in ultrafast optical spectroscopy of perovskites is absolutely essential for uncovering their intrinsic photophysical properties. Femtosecond TAS measurements with selective 400 nm and 600 nm pump excitation (fluence < 1.3 μJ cm^{-2}) and a white-light continuum (WLC) probe uncovered a slow 0.4 ps hot hole cooling process from a deeper valence band level (VB2) to the valence bandedge (VB1) – see Fig. 7. With careful tailoring of the HTM's energy levels, one could efficiently extract these hot hole energies before they cool down to VB1. Potentially, this could be utilized in perovskite solar cells to exceed the theoretical Shockley–Queisser limit.[81] Further investigations into this area should be conducted.

(b) Origins of the long electron–hole diffusion lengths

The mechanism of the long electron–hole diffusion lengths in $CH_3NH_3PbI_{3-x}Cl_x$ and $CH_3NH_3PbI_3$ and their charge carrier mobilities were elucidated by L. M. Herz in collaboration with H. J. Snaith and coworkers[78] using transient THz spectroscopy and TRPL spectroscopy. Their findings show that both the monomolecular (first order, *i.e.*, from geminate recombination of excitons and/or from trap- or impurity-assisted recombination) and bimolecular (second order) charge carrier recombination rates are extremely low, with the latter defying the Langevin limit by at least four orders of magnitude. However, the Auger (third order) recombination rates were found to be high ~10^{-29} cm^6 s^{-1} – comparable to those of strongly confined colloidal quantum dots.[82] Comparatively, Auger recombination in highly-doped bulk Si wafers is ~2 orders smaller.[83] The lower bound values of the charge carrier mobilities for

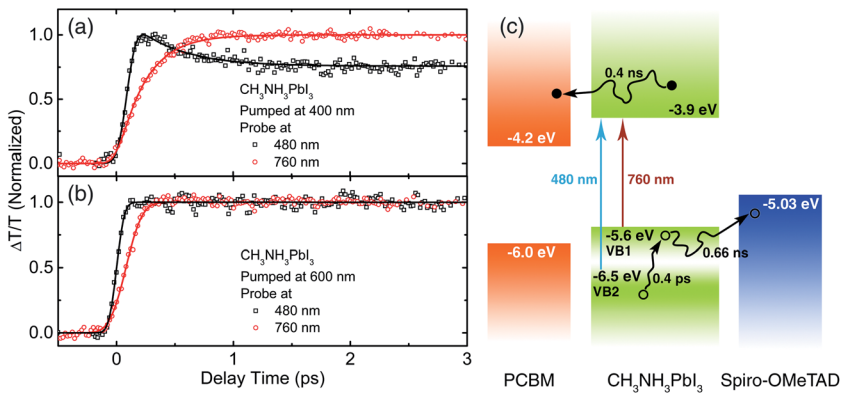

Fig. 7 Normalized bleaching kinetics at 480 and 760 nm in a short time range show the intervalence band hot hole cooling for the $CH_3NH_3PbI_3$ film (under vacuum) after excitation at (A) 400 nm (1 μJ cm^{-2}) and (B) 600 nm (1.3 μJ cm^{-2}). (C) A schematic illustrating the hot-hole cooling and charge recombination within $CH_3NH_3PbI_3$ and charge separation at the $CH_3NH_3PbI_3$/PCBM and $CH_3NH_3PbI_3$/spiro-OMeTAD interfaces. The approximate positions of VB1 and VB2 were obtained from the TA measurements. Reproduced with permission from ref. 46, copyright 2013, Science (AAAS).

$CH_3NH_3PbI_{3-x}Cl_x$ and $CH_3NH_3PbI_3$ were determined to be 11.6 $cm^2\ V^{-1}\ s^{-1}$ and ~8 $cm^2\ V^{-1}\ s^{-1}$, respectively, which are extremely high for the solution-processed perovskites. Comparatively, these values are >20 times larger than that of mesoporous TiO_2 and several orders larger than those of typical π-conjugated molecular semiconductors. The origins of the long electron–hole diffusion lengths stem from the novel combination of low charge carrier recombination rates and high charge carrier mobilities in these perovskites.

(c) Summary of photophysical processes in pristine films

A generalized scheme of the dynamic interplay of the various photophysical processes and loss mechanisms in bare perovskite thin films following photoexcitation is shown in Fig. 8. Absorption of photons results in the generation of electron–hole pairs that evolve towards the formation of highly delocalized Wannier excitons after thermalization. A fraction of which would dissociate spontaneously back into free carriers. The excitons and free carriers coexist and their dynamic populations continue to vary over their lifetimes. Geminate recombination of the excitons, or the recombination involving an electron and a hole generated from the quenching of a single exciton is inefficient. Likewise, trap-assisted recombination, another monomolecular process, is also suppressed in these $CH_3NH_3PbX_3$ perovskites. At stronger light intensities, non-geminate recombination originating from the recombination of two free charges (*i.e.*, bimolecular in nature) is extremely low – defying the traditional Langevin limit by at least four orders of magnitude. Auger recombination (involving a three particle process) on the other hand is dominant in $CH_3NH_3PbX_3$ perovskites and surprisingly, ASE even occurs at higher pump excitations – out-competing the Auger processes in $CH_3NH_3PbI_3$.[80] Eventually, in these bare perovskite films without a HTM and in the absence of any charge extraction, the photoexcited species (excitons and free carriers) undergo radiative (luminescence) or non-radiative processes within the perovskite. It is also important to note that under solar light intensities (low intensity excitation), Auger recombination or ASE would be strongly suppressed. With the non-radiative pathways (geminate recombination, trap-assisted recombination and Auger recombination) weak or inactive under solar light intensities, it is therefore understandable that these perovskites make excellent photovoltaic materials.

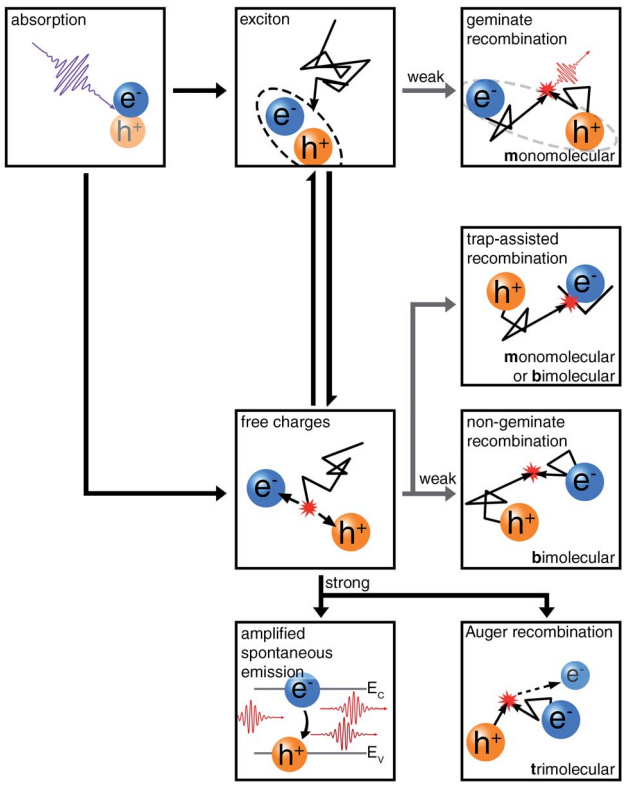

Fig. 8 A schematic of the photophysical processes and loss mechanisms in perovskites following photoexcitation. Efficient (or strong) pathways and suppressed (or weak) pathways are denoted by the black and grey lines, respectively. Monomolecular recombination is charge carrier density independent, while bimolecular and Auger recombination are charge carrier density dependent processes that would typically be present under high intensity photoexcitation. In fact, under even higher photoexcitation densities, amplified spontaneous emission (ASE) will out-compete Auger recombination. However, under solar light intensities (low intensity excitation), these latter processes will be strongly suppressed.

5. Charge transfer mechanisms in perovskite solar cells

As described previously, various configurations of perovskite solar cells have been explored. These include the configurations where the perovskite is interfaced with mesoporous TiO_2, mesoporous Al_2O_3 (MSSC) as well as other organic electron and hole transport layers. Ultrafast measurements have clearly indicated that $CH_3NH_3PbI_3$ and $CH_3NH_3PbI_{3-x}Cl_x$, both have long and balanced electron–hole transport lengths.[46,77] It has also been clearly shown that injection into electron acceptors such as PCBM and hole transporters such as PEDOT:PSS and spiro-OMeTAD is efficient.[46,53,59,77] Thus, planar configurations of perovskite solar cells can be expected to function as thus: under photoexcitation, a mixture of weakly bound excitons and direct electron and hole generation occurs. Due to the crystalline nature of the perovskite as well as low trap densities, the recombination within the perovskites is limited. The long-lived nature of electrons and holes allows them to be collected by electron and hole acceptor layers, before making their way out of the solar cells as photocurrent. The high open circuit voltages noted in such planar configurations also point to a scenario where energetic costs associated with exciton splitting is not prevalent. Light intensity dependent measurements on a PEDOT:PSS/$CH_3NH_3PbI_{3-x}Cl_x$/PCBM solar cell indicate that the main recombination mechanism is free carrier recombination.[59] The meso-superstructured solar cells[33,36,50,51] which utilize an insulating mesoporous layer as a scaffold for the perovskite can be expected to work in a similar manner. Here the primary charge separation interface is at the perovskite/hole transporting layer (spiro-OMeTAD) into which

hole injection occurs efficiently. The good electron transport properties of the perovskite layer ensure that electrons are collected through the compact TiO_2 layer below the insulating mesoporous layer. Thus, a connected perovskite layer within the mesoporous layer is critical. The exact working principle behind solar cells fabricated by depositing the perovskite on a mesoporous TiO_2 layer is still not clearly established. The pertinent questions when considering this architecture are: (a) is there injection of electrons from the perovskite into mesoporous TiO_2; (b) is the more efficient path for electron collection through the mesoporous TiO_2 or within the perovskite itself? (c) Which pathway results in higher extraction efficiency in the perovskite solar cell?

N. G. Park in collaboration with M. Grätzel and coworkers[32] published the earliest study on the dynamics of the charge separation processes in $CH_3NH_3PbI_3/TiO_2$ solar cells probed using femtosecond transient absorption spectroscopy (fs-TAS). However, clear evidence of efficient electron injection into TiO_2 could not be observed due to the overlapping signals from the stimulated emission from the perovskite. Although the question on whether perovskite can inject electrons into the mesoporous TiO_2 has more or less been answered by photoinduced absorption spectroscopy (PIA) from the evidence of a broad absorption feature in the region ~1.1 μm attributed to free electrons in the titania from $CH_3NH_3PbI_{3-x}Cl_x$,[33,85] clear evidence of efficient injection remains elusive. Most recently, J.-E. Moser in collaboration with M. Grätzel and coworkers unravelled the mechanism of the charge transfer processes in perovskite solar cells (Fig. 9(a)) and presented clear evidence of not only efficient electron injection from photoexcited $CH_3NH_3PbI_3$ into TiO_2, but also efficient hole injection from photoexcited $CH_3NH_3PbI_3$ into the HTM (spiro-OMeTAD) occurring simultaneously over comparable ultrafast timescales (≤3 ps).[84] They had overcome the challenges of a spectral overlap encountered in the earlier study[32] by probing in the infrared (1.4 μm) which allows direct observation of only the carrier's population decay within the perovskite itself (Fig. 9(b)).

The second and third questions on whether electron collection is more efficient through the mesoporous TiO_2 or within the perovskite itself; and which pathway results in higher extraction efficiency in perovskite solar cells remains open. H. J. Snaith in collaboration with T. N. Murakami and T. Miyasaka and coworkers[33] showed using transient photocurrent measurements that the charge collection in the insulating Al_2O_3-based devices is faster than the TiO_2-based devices – indicating that the perovskite material itself is more efficient in transporting the negative charge than mesoporous TiO_2. However, recent findings by Marchioro *et al.* using transient absorption spectroscopy showed that the amount of long-lived charges in the $TiO_2/CH_3NH_3PbI_3$/HTM samples is higher than that in the $Al_2O_3/CH_3NH_3PbI_3$/HTM samples (Fig. 9(b)) – indicating a more efficient charge separation in the former. Furthermore, charge recombination with oxidized HTM species was also found to be slower on TiO_2 films compared to Al_2O_3 films (Fig. 9(c)). The efficiency of charge extraction in a perovskite solar cell also depends on the ratio between charge recombination and charge separation rates. Nevertheless,

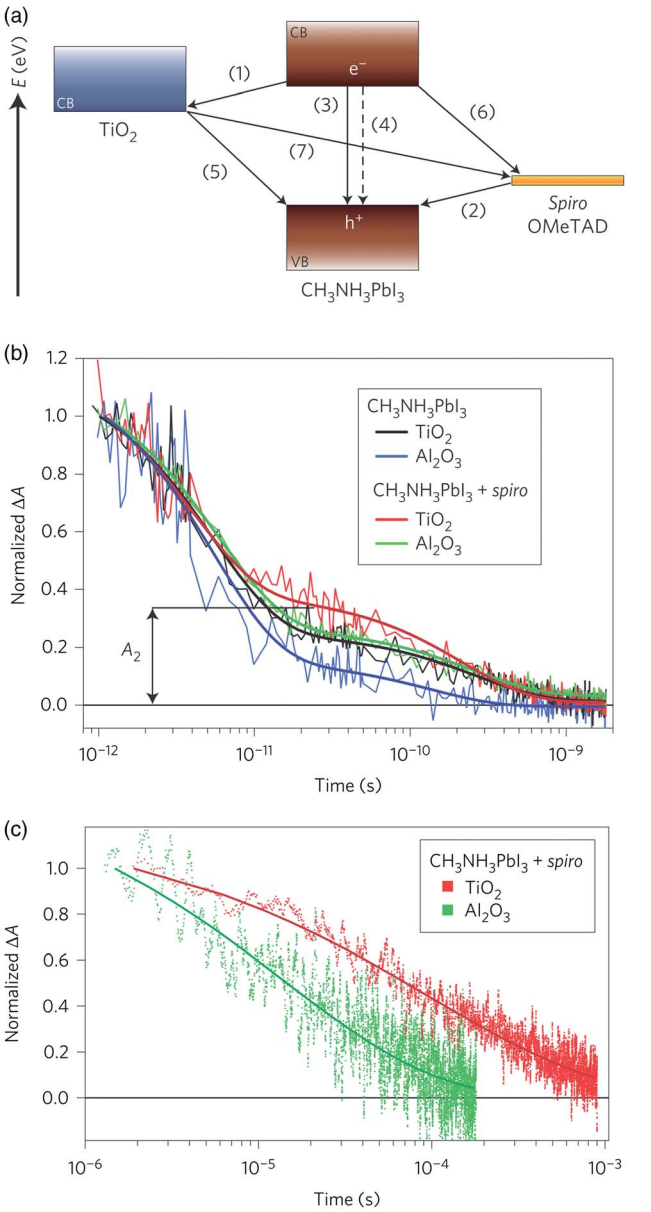

Fig. 9 (a) Schematic diagram of energy levels and electron transfer processes in an HTM/perovskite/TiO_2 cell. (1) Electron injection; (2) hole injection; (3) radiative exciton recombination; (4) non-radiative exciton recombination; (5) back electron transfer at the TiO_2 surface; (6) back charge transfer at the HTM surface; (7) charge recombination at the TiO_2/HTM interface. (b) Transient absorption signals were measured at a probe wavelength of 1.4 μm following the femtosecond laser pulsed excitation at 580 nm: $CH_3NH_3PbI_3$ on TiO_2 (black); $CH_3NH_3PbI_3$ on Al_2O_3 (blue); $CH_3NH_3PbI_3$ and spiro-OMeTAD on TiO_2 (red); $CH_3NH_3PbI_3$ and spiro-OMeTAD on Al_2O_3 (green). Thick solid lines represent bi-exponential fits of experimental points starting at $t = 1$ ps. A_2 represents the normalized absorbance change at 25 ps, used as a metric to compare the various samples. (c) Samples with a HTM. Signals mainly reflect the decay of the h^+ (HTM) population. $CH_3NH_3PbI_3$ and spiro-OMeTAD on TiO_2 (red); $CH_3NH_3PbI_3$ and spiro-OMeTAD on Al_2O_3 (green). Thick lines represent stretched exponential fit of data. Reproduced with permission from ref. 84, copyright 2014, Nature Publishing Group.

Marchioro *et al.*'s findings showed that it is advantageous to use TiO_2 as the electron acceptor and transporter, together with a HTM in perovskite solar cells – providing only partial answers to question 3.

Impedance spectroscopy measurements have also been applied to perovskite solar cells in a bid to understand the electrical processes occurring in them. Bisquert and coworkers analysed perovskite solar cells on TiO_2 and ZrO_2 and proposed that carrier accumulation occurs in the perovskite layers.[86] This indicates that the working principle of the perovskite solar cells is different from that of a pure DSSC where instantaneous injection from the dye into the TiO_2 occurs and no charge accumulation is observable in the light absorber. Dualeh *et al.* in their impedance spectroscopy analysis have argued that the observation of the mesoporous TiO_2 chemical capacitance in perovskite solar cells indicates that the electron transport is channeled through the mesoporous TiO_2.[87] The capacitance of TiO_2 in perovskite solar cells has also been observed by Abrusci *et al.* in their differential capacitance measurements when employing a C_{60}-self assembled monolayer on top of the TiO_2 surface.[85] Zhu and coworkers also point to a similar working mechanism in solid state DSCs and perovskite solar cells dominated by electron transport within the mesoporous TiO_2 layer itself, from intensity modulated photocurrent/photovoltage spectroscopy (IMPS/IMVS) measurements.[88] However Bisquert and coworkers have reported a similar impedance spectral shape in planar $CH_3NH_3PbI_{3-x}Cl_x$ and nanostructured $CH_3NH_3PbI_3$ solar cells. Since there is an absence of the TiO_2 mesoporous layer in one of the devices, they attribute the features in the impedance spectra to charge transport and recombination processes occurring within the perovskite layer solely. The authors have also noted that more complicated impedance spectral patterns can be observed in other cases which necessitates the development of a complete model.

The unclear view of the exact working principles of perovskite-mesoporous TiO_2 solar cells could stem from the variations in the solar cell structures studied and their ensuing interfacial charge transfer dynamics. The impact of the degree of coverage of the mesoporous TiO_2 by the perovskite is unclear. The presence or absence of a perovskite overlayer on the mesoporous TiO_2 will modulate the recombination at the perovskite/TiO_2/HTM interfaces. Additionally the distribution of the perovskite within the TiO_2 pores may also play a defining role in what mechanism of electron transport dominates. For example, the charge transport time in $CH_3NH_3PbI_3$ formed from the sequential deposition process was found to be 3 times longer than that obtained from the single precursor spincoating process.[36] From spectroscopic evidence, it is clear that charge injection from perovskite into mesoporous TiO_2 is possible;[33,84,85] however, the exact ratio between electrons being transported through the mesoporous TiO_2 and that transported through the perovskite is unknown. Possibly, spectroscopic measurements in working solar cells at different applied voltages may unravel this question.

6. Future directions and open questions in the field

In the wake of the rapidly expanding field, several pressing open questions remain. They have been largely swept aside in the initial surge for high efficiencies. As the perovskite photovoltaic field matures, these gaps in our understanding need to be progressively tackled and filled:

(a) Interfacial charge transfer dynamics

For any given material system, factors such as device processing and the ensuing morphology and coverage can strongly affect the carrier dynamics and the device performance. Systematic studies into understanding the morphological effects arising from the single precursor *vs.* sequential deposition solution-processed approach or thermal evaporation approach on the charge dynamics in pristine and heterojunction perovskite films are urgently needed. Given that the 100 nm e–h diffusion lengths estimated from the single step processed $CH_3NH_3PbI_3$ are *minimum values*,[46] further work is urgently needed to carefully examine the e–h diffusion lengths in sequential deposited films and evaporated films to establish their upper limits. Over the next phase of development in this field, one can look forward to an upsurge of systematic transient spectroscopy studies of various pristine/heterojunction configurations over the entire charge generation to charge extraction timescale, in particular: (i) the dynamic interplay and interactions between the excitons and the free charge population and their effects on the charge separation, recombination and transport; (ii) the interfacial charge dynamics and the mechanism of the charge injection at the perovskite/mesoporous TiO_2; perovskite/semiconductor nanostructure; and perovskite/graphene interfaces; and (iii) the exact role of higher lying states (if any) for charge separation. Time-resolved optical pump–terahertz probe spectroscopy would be extremely useful to monitor the early time excitons and free-carrier dynamics and populations in the pristine films and heterojunctions. These studies could be extended with transient microwave photoconductance measurements over longer time scales for correlation with device properties. Double excitation techniques like the pump–push probe spectroscopy can be used to study the higher lying electronic states and their roles in the charge transfer. Field modulation techniques like field assisted pump–probe spectroscopy could also lead to new insights into the interplay of the exciton dissociation and the free carrier dynamics on the charge transfer under device conditions. With the concerted efforts of various research groups, a complete picture and detailed model of the charge transfer processes of perovskite solar cells will be unravelled. Understanding the structure–function relationships in perovskite solar cells through UOS holds the key to the development of optimal solar cells with efficiencies that could surpass the 20% target.

(b) $CH_3NH_3PbI_3$ *vs.* $CH_3NH_3PbI_{3-x}Cl_x$

Highly efficient solar cells have been prepared from $CH_3NH_3PbI_3$ and $CH_3NH_3PbI_{3-x}Cl_x$. The precursor solution of

the latter compound consists of 3 parts of CH_3NH_3I for 1 part of $PbCl_2$. Although initial studies had termed the mixed composition as $CH_3NH_3PbI_2Cl$, the crystallographical and optical absorption properties are identical to that of $CH_3NH_3PbI_3$.[33] Stranks *et al.* have shown that[77] the diffusion lengths measured in $CH_3NH_3PbI_{3-x}Cl_x$ are significantly longer than that in $CH_3NH_3PbI_3$, although the device performance of both compositions are comparable. In addition, while the charge carrier mobilities in both $CH_3NH_3PbI_{3-x}Cl_x$ and $CH_3NH_3PbI_3$ are similar, the bimolecular recombination rates in the mixed halide system are approximately one order lower, suggesting that electronic structure modulation by Cl has a role in reducing the spatial overlap of the electron and holes.[78] Colella *et al.* have also proposed that Cl within $CH_3NH_3PbI_3$ can act as a dopant, improving the transport properties.[89] XPS measurements have revealed that the final composition of the $CH_3NH_3PbI_{3-x}Cl_x$ contains a significantly low amount of Cl (Cl/Cl + I = 2.2%) within them.[59] XRD analysis of evaporated $CH_3NH_3PbI_{3-x}Cl_x$ films[55] also revealed impurity peaks of PbI_2, although the precursors were $PbCl_2$ and CH_3NH_3I. This points to the Cl source (either $PbCl_2$ or CH_3NH_3Cl) playing a role in the film formation. The development of a preferred orientation in $CH_3NH_3PbI_{3-x}Cl_x$ films[33] in contrast to $CH_3NH_3PbI_3$ films[35] again indicates that the Cl plays a role in film formation. Studies on $CH_3NH_3PbI_3$ and $CH_3NH_3PbI_{3-x}Cl_x$ films with similar film properties (morphological and crystallographical) are required to reveal the electronic role of Cl within the perovskite.

(c) Hole transporting layers

The hole transporting material of choice for perovskite solar cells is spiro-oMeTAD, which has been well studied due to its popularity in solid-state DSCs. However, the high commercial prices of spiro-oMeTAD (due to synthesis complexity) as well as its tendency to be uncontrollably doped by O_2, necessitate the development of alternatives. The wide variety of hole transporting organic layers originally developed for organic thin film transistors as well as light emitting devices could possibly be applied in conjunction with the perovskite system. An early study on alternatives to spiro-oMeTAD for perovskite solar cells had indicated that thiophene based systems may not be suitable.[34] Arylamine based hole transporters such as poly-triarylamine,[34] *N*,*N*-di-*p*-methoxyphenylamine-substituted pyrene derivatives[90] and swivel cruciform thiophene-based molecules[91] have shown performances between 11 and 12%. An interesting development[92] has been the utilisation of the inorganic CuI hole transport layer with $CH_3NH_3PbI_3$. Although they performed worse than spiro-oMeTAD solar cells due to high recombination, the work does indicate the possibility of applying other inorganic hole transporters such as CuSCN to the perovskite system. An equally intriguing avenue is the application of nanocarbon (*e.g.* graphite, carbon nanotubes, graphene/polymer composites) based hole transporters. As has been pointed out by Johansson and coworkers, the efficiencies can be primarily determined by recombination at the perovskite–HTM interface.[76] The low thicknesses of HTM layers (~100 nm) in well optimised solar cells as well as the utilisation of dopants point to very low losses within the HTM itself, indicating the crucial nature of the perovskite–HTM interaction.

(d) Newer perovskite compositions

Much of the high efficiency solar cells have utilised $CH_3NH_3PbI_3$ as the light absorber. Although this composition currently yields the most efficient solar cells, newer perovskite compositions which have tuneable bandgaps would be of interest to tandem solar cell configurations or in power applications that require high voltages. Seok and coworkers have elegantly shown how partial substitution of I with Br can yield colourful solar cells with varying photocurrent onset. One benefit of the partial substitution seems to be improved stability.[37] Similarly, Hodes and Cohen have demonstrated $CH_3NH_3PbBr_{3-x}Cl_x$ solar cells with open circuit voltages as high as 1.5 V.[93] Another key effort required is the reduction of the bandgap of the perovskite solar cells for increased spectral response and therefore improved efficiencies. $CH_3NH_3PbI_3$ based solar cells do not efficiently harvest photons close to its optical absorption onset (600–780 nm), resulting in photocurrents not approaching the theoretical maximum. The development of formamidinium ($HC(NH_2)_2^+$) lead perovskites[94–97] with a lower bandgap (1.48 eV) that allows for high photocurrents is thus a promising development. These high photocurrents allowed Eperon *et al.* to demonstrate planar heterojunction solar cells with power conversion efficiencies of up to 14.2%.[94] The most pressing demand for newer photoactive perovskites is driven by the need to replace Pb. Hodes has estimated that a production capacity of 1000 GW per year from $CH_3NH_3PbI_3$ solar cells requires less than 10 000 tons of lead – much lower than the 4 million tons per year of lead used for lead-acid batteries currently.[98] Thus, although the total amount of lead that is required is low, the risk of leaching Pb into the environment needs to be managed. Sn^{2+} may serve as a replacement to Pb^{2+}, but its tendency to be easily oxidised is a drawback.[99] Computational predictions play a critical role in Pb replacement efforts, due to the large variety of halide perovskites possible.

(e) Towards printability and scalability

The rapid growth in the efficiencies of perovskite solar cells within a short time period has been catalogued previously.[98,100] A target of 20% PCE value has also been identified as attainable in the perovskite solar cells. However, as important as the quest for efficiency is the pursuit of development activities aimed at depositing the perovskite materials through scalable manufacturing techniques such as screen printing. Carnie *et al.* have demonstrated that Al_2O_3 nanoparticles can be mixed directly with perovskite solution and spuncoated to form a composite photoactive layer.[51] Further development of similar process recipes could yield compositions that could be screen printed, blade coated or applied through slot die coating. A fully printable perovskite solar cells albeit with an unconventional device configuration has been demonstrated by Han and coworkers.[101] The device architecture consisted of a screen

printed TiO_2 layer, a ZrO_2 layer and a carbon black/graphite composite layer onto which $CH_3NH_3PbI_3$ was dropcast. Such devices displayed an efficiency of 6.64%. A critical barrier in the implementation of a printable perovskite solar cell is the deposition of the electron selective compact layer (typically TiO_2 formed by spray pyrolysis at high temperature). Planar perovskite solar cells employing organic electron and hole transport layers do not suffer from this limitation, but still display lower efficiencies than mesoporous layer based solar cells.[45,53,58,59,62] Approaches to avoid the high temperature processes during the formation of the compact layer includes the utilization of electrodeposited ZnO[41] or a spuncoated ZnO nanoparticle layer.[57] A similar nanoparticle based approach has been demonstrated by the utilization of a spuncoated graphene flake/TiO_2 nanoparticle layer as the compact layer – yielding efficiencies of 15.6%.[102] Very recently, a new low temperature compact layer TiO_2 deposition recipe has yielded impressive efficiencies of up to 15.9% for a solar cell fabricated at temperatures less than 150 °C.[103]

Much of the high efficiency reports on perovskite solar cells have been demonstrated on cell areas much less than 1 cm^2 (Table 2). Malinkiewicz *et al.* who reported an efficiency of 12.04% (cell area = 0.09 cm^2) fabricated an ~1 cm^2 solar cell using the same process which yielded an efficiency of 8.27%.[62] The primary difference in the photovoltaic parameters was the FF which reduced from 0.67 to 0.52 when going to the larger area solar cells. The reason for the reduction in the FF is unclear, but could arise from series resistance in the electrode itself. The first perovskite based modules have also been reported (up to 16.8 cm^2 module area) by Matteocci *et al.* who employed both P3HT and spiro-OMeTAD as hole transporters yielding efficiencies of 5.1%.[104] Such large scale demonstrations of perovskite solar cells are necessary for perovskite solar cells to develop into a technology for widespread deployment.

(f) Stability studies

The 3-D methylammonium trihalogenoplumbates (II) crystals (*i.e.*, $CH_3NH_3PbCl_3$, $CH_3NH_3PbBr_3$ and $CH_3NH_3PbI_3$) are known to undergo 1st order phase transitions.[105,106] In particular, $CH_3NH_3PbI_3$ undergoes a tetragonal I to cubic phase transition at ~327 K (or ~54 °C), which is close to the device operating temperatures under direct sunlight. This cubic–tetragonal transition results in the methylammonium ions exhibiting a disordered character while the PbX_6 octahedron exhibits a displacive character.[106,107] Systematic studies of such effects on the carrier dynamics and on the device properties under operation are warranted. Since the phase transitions involve a volume change, it is pertinent to investigate whether infiltrating the perovskite within mesoporous layers can improve temperature stability. Reports on long term device performance tests are few, with 500 h stabilities under constant illumination being reported by Grätzel and coworkers.[35] Snaith and coworkers have reported performance data for 1000 h in MSSCs and have pointed towards UV induced changes in TiO_2 based solar cells due to desorption of surface-adsorbed oxygen.[108] Systematic studies on the degradation mechanisms (including the hole transport layers) are required to manage the lifetimes of these solar cells. Newer perovskite compositions which do not undergo phase transitions at device operational temperatures should be pursued as well.

In summary, the field of perovskite solar cells has rapidly grown to become the most efficient solution processed photovoltaics, leapfrogging other 3rd generation photovoltaic technologies. As this field matures, rapid improvements in the

Table 2 Compilation of high efficiency perovskite solar cells reported thus far (1st February 2014)

Report	Device structure	Device parameters	Efficiency	Active area
Sub-150 °C processed meso-superstructured perovskite solar cells with enhanced efficiency, *Energy Environ.l Sci.* 2014, **7**, 1142–1147	FTO/TiO_2/mesoporous Al_2O_3/$CH_3NH_3PbI_{3-x}Cl_x$/spiro-OMeTAD/Ag	J_{sc} = 21.5 mA cm^{-2}, V_{oc} = 1.02 V and FF = 0.71	15.9%	0.0625 cm^2
Perovskite solar cells with a planar heterojunction structure prepared using room-temperature solution processing techniques. *Nat. Photonics* 2014, **8**, 133–138	ITO/ZnO/$CH_3NH_3PbI_3$/spiro-OMeTAD/Ag	J_{sc} = 20.4 mA cm^{-2}, V_{oc} = 1.03 V and FF = 0.749	15.7%	0.07065 cm^2
Low-temperature processed electron collection layers of graphene/TiO_2 nanocomposites in thin film perovskite solar cells, *Nano Lett.* 2014, **14**, 724–730	FTO/graphene–TiO_2/mesoporous-Al_2O_3/$CH_3NH_3PbI_{3-x}Cl_x$/spiro-OMeTAD/Au	J_{sc} = 21.9 mA cm^{-2}, V_{oc} = 1.04 V and FF = 0.73	15.6%	0.0625 cm^2
Efficient planar heterojunction perovskite solar cells by vapour deposition, *Nature* 2013, **501**, 395–398	FTO/TiO_2/$CH_3NH_3PbI_{3-x}Cl_x$/spiro-OMeTAD/Ag	J_{sc} = 21.5 mA cm^{-2}, V_{oc} = 1.07 V and FF = 0.67	15.4%	0.076 cm^2
Sequential deposition as a route to high-performance perovskite-sensitized solar cells, *Nature* 2013, **499**, 316–319	FTO/TiO_2/mesoporous TiO_2/$CH_3NH_3PbI_3$/spiro-OMeTAD/Au	J_{sc} = 20 mA cm^{-2}, V_{oc} = 0.993 V and FF = 0.73 J_{sc} = 21.3 mA cm^{-2}, V_{oc} = 1.0 V and FF = 0.66	15.0% 14.1% (certified)	0.285 cm^2 0.209 cm^2

power conversion efficiencies will become harder to come by. Thus, a deeper understanding of the fundamental working mechanisms become increasingly important especially if efficiencies exceeding 20% need to be achieved. Concurrently, technological developments in the area of scalable manufacturing techniques, toxicity and stability need to be effectively addressed.

Acknowledgements

We would like to acknowledge Subodh Mhaisalkar and Pablo P. Boix for technical discussions and Tom Baikie and Swee Sien Lim for the figures. T.C.S. acknowledges the financial support from NTU start-up grant M4080514, SPMS collaborative Research Award M4080536 and Ministry of Education AcRF Tier 2 grant MOE2013-T2-1-081. N.M. acknowledges the financial support from NTU start-up grant M4081293 and from Singapore National Research Foundation (NRF) through the Competitive Research Program (NRF-CRP4-2008-03). T.C.S. and N.M. also gratefully acknowledge the Singapore NRF for the funding through the Singapore-Berkeley Research Initiative for Sustainable Energy (SinBeRISE) CREATE Programme.

References

1 J. Nelson, *The Physics of Solar Cells*, Imperial College Press, 2003.
2 X. Wang, J. Byrne, L. Kurdgelashvili and A. Barnett, *Wiley Interdiscip. Rev.: Energy Environ.*, 2012, **1**, 132–151.
3 D. B. Mitzi, in *Progress in Inorganic Chemistry*, John Wiley & Sons, Inc., 2007, pp. 1–121, DOI: 10.1002/9780470166499.ch1.
4 T. Ishihara, *Optical Properties of Pb-based inorganic–organic perovskites*, World Scientific, Singapore, River Edge, NJ, 1995, p. xix, 414 p.
5 K. A. Müller and T. W. Kool, *Properties of perovskites and other oxides*, World Scientific, Singapore, Hackensack, NJ, 2010.
6 T. Ishihara, J. Takahashi and T. Goto, *Solid State Commun.*, 1989, **69**, 933–936.
7 I. B. Koutselas, L. Ducasse and G. C. Papavassiliou, *J. Phys.: Condens. Matter*, 1996, **8**, 1217–1227.
8 C. R. Kagan, D. B. Mitzi and C. D. Dimitrakopoulos, *Science*, 1999, **286**, 945–947.
9 D. B. Mitzi, K. Chondroudis and C. R. Kagan, *IBM J. Res. Dev.*, 2001, **45**, 29–45.
10 X. Hong, T. Ishihara and A. V. Nurmikko, *Solid State Commun.*, 1992, **84**, 657–661.
11 M. Era, S. Morimoto, T. Tsutsui and S. Saito, *Appl. Phys. Lett.*, 1994, **65**, 676–678.
12 C. Q. Xu, T. Kondo, H. Sakakura, K. Kumata, Y. Takahashi and R. Ito, *Solid State Commun.*, 1991, **79**, 245–248.
13 T. Kondo, S. Iwamoto, S. Hayase, K. Tanaka, J. Ishi, M. Mizuno, K. Ema and R. Ito, *Solid State Commun.*, 1998, **105**, 503–506.
14 A. Brehier, R. Parashkov, J. S. Lauret and E. Deleporte, *Appl. Phys. Lett.*, 2006, **89**, 171110.
15 T. Leijtens, G. E. Eperon, S. Pathak, A. Abate, M. M. Lee and H. J. Snaith, *Nat. Commun.*, 2013, **4**, 2885.
16 G. Lanty, S. Zhang, J. S. Lauret, E. Deleporte, P. Audebert, S. Bouchoule, X. Lafosse, J. Zuniga-Perez, F. Semond, D. Lagarde, F. Medard and J. Leymarie, *Phys. Rev. B: Condens. Matter Mater. Phys.*, 2011, **84**, 195449.
17 Z. Han, H. S. Nguyen, F. Boitier, Y. Wei, K. Abdel-Baki, J. S. Lauret, J. Bloch, S. Bouchoule and E. Deleporte, *Opt. Lett.*, 2012, **37**, 5061–5063.
18 Y. Wei, J. S. Lauret, L. Galmiche, P. Audebert and E. Deleporte, *Opt. Express*, 2012, **20**, 10399–10405.
19 G. C. Papavassiliou, *Prog. Solid State Chem.*, 1997, **25**, 125–270.
20 S. M. Wang, D. B. Mitzi, C. A. Feild and A. Guloy, *J. Am. Chem. Soc.*, 1995, **117**, 5297–5302.
21 Y. Kawamura, H. Mashiyama and K. Hasebe, *J. Phys. Soc. Jpn.*, 2002, **71**, 1694–1697.
22 B. R. Vincent, K. N. Robertson, T. S. Cameron and O. Knop, *Can. J. Chem.*, 1987, **65**, 1042–1046.
23 T. Umebayashi, K. Asai, T. Kondo and A. Nakao, *Phys. Rev. B: Condens. Matter Mater. Phys.*, 2003, **67**, 155405.
24 Y. H. Chang, C. H. Park and K. Matsuishi, *J. Korean Phys. Soc.*, 2004, **44**, 889–893.
25 E. Mosconi, A. Amat, M. K. Nazeeruddin, M. Gratzel and F. De Angelis, *J. Phys. Chem. C*, 2013, **117**, 13902–13913.
26 T. Baikie, Y. N. Fang, J. M. Kadro, M. Schreyer, F. X. Wei, S. G. Mhaisalkar, M. Graetzel and T. J. White, *J. Mater. Chem. A*, 2013, **1**, 5628–5641.
27 Y. Wang, T. Gould, J. F. Dobson, H. Zhang, H. Yang, X. Yao and H. Zhao, *Phys. Chem. Chem. Phys.*, 2014, **16**, 1424–1429.
28 J. Even, L. Pedesseau, J. M. Jancu and C. Katan, *J. Phys. Chem. Lett.*, 2013, **4**, 2999–3005.
29 B. O'Regan and M. Grätzel, *Nature*, 1991, **353**, 737–740.
30 A. Kojima, K. Teshima, Y. Shirai and T. Miyasaka, *J. Am. Chem. Soc.*, 2009, **131**, 6050–6051.
31 J. H. Im, C. R. Lee, J. W. Lee, S. W. Park and N. G. Park, *Nanoscale*, 2011, **3**, 4088–4093.
32 H. S. Kim, C. R. Lee, J. H. Im, K. B. Lee, T. Moehl, A. Marchioro, S. J. Moon, R. Humphry-Baker, J. H. Yum, J. E. Moser, M. Gratzel and N. G. Park, *Sci. Rep.*, 2012, **2**, 591.
33 M. M. Lee, J. Teuscher, T. Miyasaka, T. N. Murakami and H. J. Snaith, *Science*, 2012, **338**, 643–647.
34 J. H. Heo, S. H. Im, J. H. Noh, T. N. Mandal, C. S. Lim, J. A. Chang, Y. H. Lee, H. J. Kim, A. Sarkar, M. K. Nazeeruddin, M. Gratzel and S. I. Seok, *Nat. Photonics*, 2013, **7**, 487–492.
35 J. Burschka, N. Pellet, S. J. Moon, R. Humphry-Baker, P. Gao, M. K. Nazeeruddin and M. Gratzel, *Nature*, 2013, **499**, 316–319.
36 D. Bi, S.-J. Moon, L. Haggman, G. Boschloo, L. Yang, E. M. J. Johansson, M. K. Nazeeruddin, M. Gratzel and A. Hagfeldt, *RSC Adv.*, 2013, **3**, 18762–18766.
37 J. H. Noh, S. H. Im, J. H. Heo, T. N. Mandal and S. I. Seok, *Nano Lett.*, 2013, **13**, 1764–1769.
38 L. Etgar, P. Gao, Z. S. Xue, Q. Peng, A. K. Chandiran, B. Liu, M. K. Nazeeruddin and M. Gratzel, *J. Am. Chem. Soc.*, 2012, **134**, 17396–17399.

39 H.-S. Kim, J.-W. Lee, N. Yantara, P. P. Boix, S. A. Kulkarni, S. Mhaisalkar, M. Grätzel and N.-G. Park, *Nano Lett.*, 2013, **13**, 2412–2417.
40 S. Dharani, H. K. Mulmudi, N. Yantara, P. T. Thu Trang, N. G. Park, M. Graetzel, S. Mhaisalkar, N. Mathews and P. P. Boix, *Nanoscale*, 2014, **6**, 1675–1679.
41 M. H. Kumar, N. Yantara, S. Dharani, M. Graetzel, S. Mhaisalkar, P. P. Boix and N. Mathews, *Chem. Commun.*, 2013, **49**, 11089–11091.
42 D. Bi, G. Boschloo, S. Schwarzmuller, L. Yang, E. M. J. Johansson and A. Hagfeldt, *Nanoscale*, 2013, **5**, 11686–11691.
43 J. Burschka, A. Dualeh, F. Kessler, E. Baranoff, N. L. Cevey-Ha, C. Yi, M. K. Nazeeruddin and M. Grätzel, *J. Am. Chem. Soc.*, 2011, **133**, 18042–18045.
44 A. Yella, H.-W. Lee, H. N. Tsao, C. Yi, A. K. Chandiran, M. K. Nazeeruddin, E. W.-G. Diau, C.-Y. Yeh, S. M. Zakeeruddin and M. Grätzel, *Science*, 2011, **334**, 629–634.
45 S. Sun, T. Salim, N. Mathews, M. Duchamp, C. Boothroyd, G. Xing, T. C. Sum and Y. M. Lam, *Energy Environ. Sci.*, 2014, **7**, 399–407.
46 G. C. Xing, N. Mathews, S. Y. Sun, S. S. Lim, Y. M. Lam, M. Gratzel, S. Mhaisalkar and T. C. Sum, *Science*, 2013, **342**, 344–347.
47 J. J. Choi, X. Yang, Z. M. Norman, S. J. L. Billinge and J. S. Owen, *Nano Lett.*, 2013, **14**, 127–133.
48 E. Enache-Pommer, B. Liu and E. S. Aydil, *Phys. Chem. Chem. Phys.*, 2009, **11**, 9648–9652.
49 W. A. Laban and L. Etgar, *Energy Environ. Sci.*, 2013, **6**, 3249–3253.
50 J. M. Ball, M. M. Lee, A. Hey and H. J. Snaith, *Energy Environ. Sci.*, 2013, **6**, 1739–1743.
51 M. J. Carnie, C. Charbonneau, M. L. Davies, J. Troughton, T. M. Watson, K. Wojciechowski, H. Snaith and D. A. Worsley, *Chem. Commun.*, 2013, **49**, 7893–7895.
52 K. Wojciechowski, M. Saliba, T. Leijtens, A. Abate and H. J. Snaith, *Energy Environ. Sci.*, 2014, **7**, 1142–1147.
53 P. Docampo, J. M. Ball, M. Darwich, G. E. Eperon and H. J. Snaith, *Nat. Commun.*, 2013, **4**, 2761.
54 G. E. Eperon, V. M. Burlakov, P. Docampo, A. Goriely and H. J. Snaith, *Adv. Funct. Mater.*, 2014, **24**, 151–157.
55 M. Liu, M. B. Johnston and H. J. Snaith, *Nature*, 2013, **501**, 395–398.
56 Q. Chen, H. Zhou, Z. Hong, S. Luo, H.-S. Duan, H.-H. Wang, Y. Liu, G. Li and Y. Yang, *J. Am. Chem. Soc.*, 2013, **136**, 622–625.
57 D. Liu and T. L. Kelly, *Nat. Photonics*, 2013, **8**, 133–138.
58 J.-Y. Jeng, Y.-F. Chiang, M.-H. Lee, S.-R. Peng, T.-F. Guo, P. Chen and T.-C. Wen, *Adv. Mater.*, 2013, **25**, 3727–3732.
59 J. You, Z. Hong, Y. Yang, Q. Chen, M. Cai, T.-B. Song, C.-C. Chen, S. Lu, Y. Liu and H. Zhou, *ACS Nano*, 2014, **8**, 1674–1680.
60 I. K. Ding, N. Tétreault, J. Brillet, B. E. Hardin, E. H. Smith, S. J. Rosenthal, F. Sauvage, M. Grätzel and M. D. McGehee, *Adv. Funct. Mater.*, 2009, **19**, 2431–2436.
61 K. Liang, D. B. Mitzi and M. T. Prikas, *Chem. Mater.*, 1998, **10**, 403–411.
62 O. Malinkiewicz, A. Yella, Y. H. Lee, G. M. Espallargas, M. Graetzel, M. K. Nazeeruddin and H. J. Bolink, *Nat. Photonics*, 2014, **8**, 128–132.
63 R. Ito, S. Hayase, T. Kondo, S. Iwamoto, K. Ema, H. Kunugita, M. Mizuno and J. Ishi, *J. Nonlinear Opt. Phys. Mater.*, 1998, **07**, 153–159.
64 M. Shimizu and J.-I. Fujisawa, *J. Lumin.*, 2004, **108**, 189–194.
65 J. Ishi, H. Kunugita, K. Ema, T. Ban and T. Kondo, *Phys. Rev. B: Condens. Matter Mater. Phys.*, 2001, **63**, 073303.
66 N. Kitazawa, M. Aono and Y. Watanabe, *Mater. Chem. Phys.*, 2012, **134**, 875–880.
67 M. Hirasawa, T. Ishihara, T. Goto, K. Uchida and N. Miura, *Phys. B*, 1994, **201**, 427–430.
68 K. Tanaka, T. Takahashi, T. Ban, T. Kondo, K. Uchida and N. Miura, *Solid State Commun.*, 2003, **127**, 619–623.
69 T. Ishihara, *J. Lumin.*, 1994, **60-1**, 269–274.
70 M. Hirasawa, T. Ishihara and T. Goto, *J. Phys. Soc. Jpn.*, 1994, **63**, 3870–3879.
71 X. Hong, T. Ishihara and A. V. Nurmikko, *Phys. Rev. B: Condens. Matter Mater. Phys.*, 1992, **45**, 6961–6964.
72 W. Zhang, M. Saliba, S. D. Stranks, Y. Sun, X. Shi, U. Wiesner and H. J. Snaith, *Nano Lett.*, 2013, **13**, 4505–4510.
73 J. F. Muth, J. H. Lee, I. K. Shmagin, R. M. Kolbas, H. C. Casey, B. P. Keller, U. K. Mishra and S. P. DenBaars, *Appl. Phys. Lett.*, 1997, **71**, 2572–2574.
74 S. J. Zhang, P. Audebert, Y. Wei, A. Al Choueiry, G. Lanty, A. Brehier, L. Galmiche, G. Clavier, C. Boissiere, J. S. Lauret and E. Deleporte, *Materials*, 2010, **3**, 3385–3406.
75 Z. Chen, C. L. Yu, K. Shum, J. J. Wang, W. Pfenninger, N. Vockic, J. Midgley and J. T. Kenney, *J. Lumin.*, 2012, **132**, 345–349.
76 D. Bi, L. Yang, G. Boschloo, A. Hagfeldt and E. M. J. Johansson, *J. Phys. Chem. Lett.*, 2013, **4**, 1532–1536.
77 S. D. Stranks, G. E. Eperon, G. Grancini, C. Menelaou, M. J. P. Alcocer, T. Leijtens, L. M. Herz, A. Petrozza and H. J. Snaith, *Science*, 2013, **342**, 341–344.
78 C. Wehrenfennig, G. E. Eperon, M. B. Johnston, H. J. Snaith and L. M. Herz, *Adv. Mater.*, 2013, **26**, 1584–1589.
79 G. Giorgi, J.-I. Fujisawa, H. Segawa and K. Yamashita, *J. Phys. Chem. Lett.*, 2013, **4**, 4213–4216.
80 G. Xing, N. Mathews, S. S. Lim, N. Yantara, X. Liu, D. Sabba, M. Grätzel, S. Mhaisalkar and T. C. Sum, *Nat. Mater.*, 2014, **13**, 476–480.
81 C. A. Nelson, N. R. Monahan and X. Y. Zhu, *Energy Environ. Sci.*, 2013, **6**, 3508–3519.
82 V. I. Klimov, A. A. Mikhailovsky, D. W. McBranch, C. A. Leatherdale and M. G. Bawendi, *Science*, 2000, **287**, 1011–1013.
83 J. Dziewior and W. Schmid, *Appl. Phys. Lett.*, 1977, **31**, 346–348.
84 A. Marchioro, J. Teuscher, D. Friedrich, M. Kunst, R. van de Krol, T. Moehl, M. Gratzel and J.-E. Moser, *Nat. Photonics*, 2014, **8**, 250–255.

85 A. Abrusci, S. D. Stranks, P. Docampo, H.-L. Yip, A. K. Y. Jen and H. J. Snaith, *Nano Lett.*, 2013, **13**, 3124–3128.
86 H. S. Kim, I. Mora-Sero, V. Gonzalez-Pedro, F. Fabregat-Santiago, E. J. Juarez-Perez, N. G. Park and J. Bisquert, *Nat. Commun.*, 2013, **4**.
87 A. Dualeh, T. Moehl, N. Tétreault, J. Teuscher, P. Gao, M. K. Nazeeruddin and M. Grätzel, *ACS Nano*, 2013, **8**, 362–373.
88 Y. Zhao, A. M. Nardes and K. Zhu, *J. Phys. Chem. Lett.*, 2014, 490–494, DOI: 10.1021/jz500003v.
89 S. Colella, E. Mosconi, P. Fedeli, A. Listorti, F. Gazza, F. Orlandi, P. Ferro, T. Besagni, A. Rizzo, G. Calestani, G. Gigli, F. De Angelis and R. Mosca, *Chem. Mater.*, 2013, **25**, 4613–4618.
90 N. J. Jeon, J. Lee, J. H. Noh, M. K. Nazeeruddin, M. Grätzel and S. I. Seok, *J. Am. Chem. Soc.*, 2013, **135**, 19087–19090.
91 K. Thirumal, K. Fu, P. P. Boix, H. Li, T. M. Koh, W. L. Leong, S. Powar, A. C. Grimsdale, M. Gratzel, N. Mathews and S. G. Mhaisalkar, *J. Mater. Chem. A*, 2014, **2**, 6305–6309.
92 J. A. Christians, R. C. M. Fung and P. V. Kamat, *J. Am. Chem. Soc.*, 2013, **136**, 758–764.
93 E. Edri, S. Kirmayer, M. Kulbak, G. Hodes and D. Cahen, *J. Phys. Chem. Lett.*, 2014, **5**, 429–433.
94 G. E. Eperon, S. D. Stranks, C. Menelaou, M. B. Johnston, L. M. Herz and H. J. Snaith, *Energy Environ. Sci.*, 2014, **7**, 982–988.
95 N. Pellet, P. Gao, G. Gregori, T.-Y. Yang, M. K. Nazeeruddin, J. Maier and M. Grätzel, *Angew. Chem., Int. Ed.*, 2014, **53**, 3151–3157.
96 T. M. Koh, K. Fu, Y. Fang, S. Chen, T. C. Sum, N. Mathews, S. G. Mhaisalkar, P. P. Boix and T. Baikie, *J. Phys. Chem. C*, 2013, DOI: 10.1021/jp411112k.
97 S. Pang, H. Hu, J. Zhang, S. Lv, Y. Yu, F. Wei, T. Qin, H. Xu, Z. Liu and G. Cui, *Chem. Mater.*, 2014, **26**, 1485–1491.
98 G. Hodes, *Science*, 2013, **342**, 317–318.
99 C. C. Stoumpos, C. D. Malliakas and M. G. Kanatzidis, *Inorg. Chem.*, 2013, **52**, 9019–9038.
100 N. G. Park, *J. Phys. Chem. Lett.*, 2013, **4**, 2423–2429.
101 Z. Ku, Y. Rong, M. Xu, T. Liu and H. Han, *Sci. Rep.*, 2013, **3**, 3132.
102 J. T.-W. Wang, J. M. Ball, E. M. Barea, A. Abate, J. A. Alexander-Webber, J. Huang, M. Saliba, I. Mora-Sero, J. Bisquert, H. J. Snaith and R. J. Nicholas, *Nano Lett.*, 2013, **14**, 724–730.
103 K. Wojciechowski, M. Saliba, T. Leijtens, A. Abate and H. Snaith, *Energy Environ. Sci.*, 2014, **7**, 1142–1147.
104 F. Matteocci, S. Razza, F. Di Giacomo, S. Casaluci, G. Mincuzzi, T. M. Brown, A. D'Epifanio, S. Licoccia and A. Di Carlo, *Phys. Chem. Chem. Phys.*, 2014, **16**, 3918–3923.
105 A. Poglitsch and D. Weber, *J. Chem. Phys.*, 1987, **87**, 6373–6378.
106 N. Onoda-Yamamuro, T. Matsuo and H. Suga, *J. Phys. Chem. Solids*, 1990, **51**, 1383–1395.
107 H. Mashiyama, Y. Kawamura, E. Magome and Y. Kubota, *J. Korean Phys. Soc.*, 2003, **42**, S1026–S1029.
108 T. Leijtens, G. E. Eperon, S. Pathak, A. Abate, M. M. Lee and H. J. Snaith, *Nat. Commun.*, 2013, **4**, 2885.